Title

Fundamental understanding of chemical processes in extreme ultraviolet resist materials

Permalink

https://escholarship.org/uc/item/50h4g627

Journal

The Journal of Chemical Physics, 149(15)

ISSN

0021-9606

Authors

Kostko, Oleg
Xu, Bo
Ahmed, Musahid
et al.

Publication Date

2018-10-21

DOI

10.1063/1.5046521

Peer reviewed

Fundamental understanding of chemical processes in extreme ultraviolet resist materials

Oleg Kostko,[1] Bo Xu,[1] Musahid Ahmed,[1] Daniel S. Slaughter,[1] D. Frank Ogletree,[2] Kristina D. Closser,[2] David G. Prendergast,[2] Patrick Naulleau,[3] Deirdre L. Olynick,[2] Paul D. Ashby,[2] Yi Liu,[2] William D. Hinsberg,[4] Gregory M. Wallraff[5]

[1]Chemical Sciences Division, Lawrence Berkeley National Laboratory, Berkeley, CA, USA
[2]Molecular Foundry, Lawrence Berkeley National Laboratory, Berkeley, CA, USA
[3]Center for X-Ray Optics, Lawrence Berkeley National Laboratory, Berkeley, CA, USA
[4]Columbia Hill Technical Consulting, Fremont, CA, USA
[5]IBM, Almaden, CA, USA

ABSTRACT

New photoresists are needed to advance extreme ultraviolet (EUV) lithography. Tailored design of efficient photoresists is enabled by a fundamental understanding of EUV induced chemistry. Processes that occur in the resist film after absorption of an EUV photon are discussed and a novel approach to study these processes on a fundamental level is described. The processes of photoabsorption, electron emission, and molecular fragmentation were studied experimentally in the gas-phase on analogues of the monomer units employed in chemically amplified EUV resists. To demonstrate the dependence of the EUV absorption cross-section on selective light harvesting substituents, halogenated methylpenols were characterized employing the following techniques. Photoelectron spectroscopy was utilized to investigate kinetic energies and yield of the electrons emitted by a molecule. Emission of Auger electrons was detected following photoionization in the case of iodo-methylphenol. Mass-spectrometry was used to deduce the molecular fragmentation pathways following electron emission and atomic relaxation. To gain insight on the interaction of emitted electrons with neutral molecules in a condensed film, the fragmentation pattern of neutral gas-phase molecules, interacting with an electron beam was studied and observed to be similar to EUV photon fragmentation.

INTRODUCTION

Photolithography[1–4] is used to manufacture the vast majority of today's integrated circuits. In this process, the demagnified image of a circuit pattern created by transmitting or reflecting light from a mask is projected onto a silicon wafer. This image is recorded in a light-sensitive photoresist film and ultimately etched into the silicon wafer. The patterning resolution of this process is primarily limited by the wavelength of light used in the lithography. To continue the push to ever smaller feature sizes, the industry is now transitioning from deep ultraviolet (DUV) light (at 248 and 193 nm) to extreme ultraviolet (EUV) lithography systems[4–8] at a wavelength of only 13.5 nm (corresponding to photon energy of 92 eV). The development of photoresists capable of simultaneously meeting the resolution, sensitivity, and fidelity requirements necessary for imaging at feature sizes below 20 nm remains one of the key challenges facing the long term success of semiconductor lithography. This is complicated by the fact that the imaging mechanism in EUV resists is substantially different than that of DUV lithography. Consequently the design of EUV photoresists meeting these challenges needs to be informed by a fundamental understanding of the physical and chemical processes occurring in a photoresist film imaged with EUV radiation.

Today's state of the art DUV photoresists are based on chemically amplified (CA) resists originally developed for KrF (248 nm) based optical lithography.[9] These are mixtures of poly-hydroxystyrene polymers partially protected with acid labile protecting groups and light-activated photoacid generators (PAG's). The PAG molecule is designed to efficiently absorb the DUV light and generate acid which in turn reacts with the labile protecting groups changing the composition of the polymer in the regions exposed to light. The patterned film can then be developed provided it is soluble.

In EUV resists, due to the high energy of the incident photon (92 eV vs. 5 eV for a 248 nm photon), most of the radiation chemistry is due to emitted electrons and not the EUV photons themselves. Absorption of a 13.5 nm photon is believed to lead to processes that include the following: a) ionization of a molecule which absorbed an EUV photon, resulting in emission of a photoelectron and, in some cases, of Auger electron(s), b) fragmentation of the molecule that absorbed the photon, and c) chemical modification of surrounding molecules by the electron(s) emitted in process (a) via non-resonant (e.g. electron impact ionization and dissociation) processes and resonant (e.g. electron attachment) processes. Note that these processes occur throughout the resist film and do not involve only the PAG. Understanding all steps is crucial to harness all the deposited energy for improved patterning results.

Current lithography productivity requirements lead to a targeted EUV radiation dose of 15 mJ/cm^2, mainly imposed by the photon source development difficulties, which corresponds to only 10 EUV photons per square nm. Such a low EUV photon flux places limitations on the use of resist materials having a low EUV absorption cross-section. For example, only 15 % of the incident EUV photons are absorbed by a 30 nm poly(methyl methacrylate) (PMMA) film and 12-13 % are absorbed by a film of the same thickness of an EUV resist based on the poly-hydroxystyrene polymer and containing the PAG.[10–12] One way to improve this is to design resists incorporating high EUV cross-section elements that more efficiently utilize EUV photons via radiation absorption by core-level electrons provided that they lead to reactions that provide an effective solubility switch. Fundamental experiments can point the way to such designs.

Unfortunately, in thin condensed resist films "…it is technically nearly impossible to directly observe the reactions induced…" by absorbed EUV photons.[13] The approach used in the current study is focused on investigation of each of the elementary processes described above, employing analogues of the polymers and PAG's found in EUV CA resists. To completely isolate resist molecules from interaction with surroundings, experiments were done in the gas-phase. Mass-spectrometry and photoelectron spectroscopy techniques applied to gas-phase systems are used here to gain fundamental understanding of primary and secondary processes occurring in resist material molecules free from its surroundings, after EUV photon absorption or interaction of the molecules with electrons. We also discuss gas-phase experimental methods to probe condensed phase resist molecules towards the end of this paper.

We chose a series of commercially available halogenated methylphenols, selected to mimic the monomer units of phenolic EUV resists (see a related theory paper, providing more information on the choice of these compounds).[14] 2-methylphenol (MPh) represents the parent monomer, and four different halogen-substituted methylphenols (Hal-MPh, where Hal = F, Cl, Br, and I) were selected to investigate the effect of high cross-section substituents on the EUV processes. 2,3,5,6-tetrafluoro-4-(trifluoromethyl)phenol (C_7F_7OH), with seven fluorine atoms was chosen, to demonstrate the effect of increased loading of a high absorption cross-section element in the EUV resist. In addition, the reactivity of a PAG analogue hydroxynaphthalimide triflate (HNIT) was investigated to study dissociative electron attachment reactions, complementing recent experiments of Ptasinska *et al.*[15]

EXPERIMENTAL METHODS

Gas-phase samples were investigated using photoelectron spectroscopy, mass-spectrometry, and dissociative electron attachment techniques, which will be described in details in the corresponding subsections below.

A. Photoelectron spectroscopy

Gas-phase photoelectron spectroscopy technique, such as the velocity map imaging (VMI)[16,17]method used in this study, allows for collection of a full 4π steradian distribution of emitted electrons and for measurement of the electron's kinetic energies and angular distributions. A gas-phase VMI photoelectron spectrometer, capable of performing spectroscopy both on isolated molecules and on unsupported nanoparticles, was designed and constructed specially for this study.[18]

The Advanced Light Source (ALS), Lawrence Berkeley National Laboratory, beamlines 6.3.2 and 9.0.1 served as source of tunable EUV radiation. The possibility to tune the photon energy helps in deciphering whether the emitted electrons are primary or secondary (Auger electrons). This was done by observation of electron kinetic energy change caused by the change in photon energy for primary electrons and detecting the same kinetic energies for Auger electrons. The photon flux was determined with a photodiode (SXUV-100).

The gas-phase samples were introduced effusively either leaking their vapors in the experimental chamber if the vapor pressure of the sample material was high (MPh and Cl-MPh), or resistively heating them in an oven inside the VMI chamber (temperatures are summarized in table S1) to create partial pressure of 10^{-6} Torr.

Energy calibration of the spectrometer was performed using known spectral lines of xenon. Voltages of the spectrometer were optimized to have the best resolving power ($E/\Delta E = 32$) at kinetic energy of 50 eV. Spectral features with lower and higher kinetic energies had worse resolving power. Apart from the intrinsic resolution limitation of the VMI technique, the collected images were not ideally circular at low and high kinetic energies which resulted in additional photoelectron peaks broadening.

B. Mass-spectrometry

Time-of-flight mass-spectrometry experiments were performed on two different experimental instruments. One of them, specially designed for mass-spectrometry experiments on supersonic beams of molecules was used to collect mass-spectra of gas-phase molecules interacting with vacuum ultraviolet (VUV) radiation and with an electron beam.[19] A reflectron time-of-flight mass-spectrometer allowed the collection of mass-spectra with high resolving power of up to $m/\Delta m = 1000$. A tunable energy electron gun was utilized as a source of electrons, whereas ALS beamline 9.0.2 was used as a source of VUV radiation. Samples were introduced in a manner similar to that applied for photoelectron spectroscopy. Most of the samples were heated in an oven inside of the time-of-flight mass-spectrometer. Two samples with high vapor pressures (MPh and F-MPh) were placed in a glass bubbler and vapors were diluted by argon and injected through a 100 µm nozzle as a molecular beam with a backing pressure of 210 Torr.

A second mass-spectrometry experiment was performed with a VMI spectrometer detecting molecular cations after EUV ionization at beamline 6.3.2. The repeller electrode of the VMI spectrometer was additionally pulsed at the repetition rate of 1 kHz to provide a starting point of the time-of-flight measurement, which is needed due to the quasi-continuous nature of synchrotron radiation. The signal, amplified by a dual microchannel plate (MCP) detector was collected by a photomultiplier tube from a fast phosphor (P47) screen and averaged by a digital oscilloscope. Application of the VMI spectrometer to measure mass–spectra coupled with the detection technique (limited by the phosphor decay time) resulted in poorer mass resolving power, reaching $m/\Delta m = 30$, compared to the traditional mass-spectrometry instrument, described above. Nevertheless it served the purpose of collecting the whole set of photoelectron and mass-spectra on samples under otherwise identical conditions (number densities of molecules and photon flux).

To determine the number densities of molecules, a Near Edge X-ray Absorption Fine Structure (NEXAFS) type of measurement was performed around the carbon K edge (Fig. S1 in Supplementary information). NEXAFS spectra were obtained by collecting mass-spectra of cationic species (parents and fragments) while performing a scan of the photon energy. The sum of all mass peak intensities as a function of photon energy are shown in Fig. S1 as NEXAFS spectra. At the photon energy of 319 eV, which is about 35 eV above the carbon K edge, the intensity of the NEXAFS spectrum is unaffected by σ^*

shape resonances and is proportional to the photoionization cross-section and to the molecule's number density. Using the NEXAFS intensities of CO_2 (a gas-phase molecule with a known cross-section, leaked into the chamber) and the sample of interest at 319 eV, as well as the corresponding photoionization cross-sections, and the number density of CO_2 (found from pressure of CO_2), one can determine the number density of the samples (Table S1).

C. Dissociative electron attachment

Mass-resolved anion fragment yield measurements were performed using the LBNL dissociative electron attachment (DEA) reaction microscope, which is described in detail in an earlier paper.[20] This apparatus was used to determine the mass and yield of anion fragments formed by collisions of low-energy electrons with the target sample molecule. Electron pulses of 100 ns duration were produced at a 50 kHz repetition rate using an electron gun, with tunable (0.5-10 eV) electron beam energy distribution and a width of 0.5 eV full width at half maximum. The electron pulses were collimated using a combination of electrostatic lenses within the electron gun and a uniform magnetic field, produced by Helmholtz coils coaxial to the electron beam direction. The magnetic field also served to contain scattered electrons near the common axis of the Helmholtz coils and the pulsed electron beam, thus separating the scattered electron background from the dissociating anion fragments resulting from dissociative electron attachment.

The target samples in the latter experiment, 4-iodo-2-methylphenol (I-MPh) or n-hydroxynaphthalimide triflate (HNIT), were contained in a crucible of a restively heated oven inside the vacuum chamber and heated to a temperature of 150 ^{o}C. An effusive molecular beam was formed by allowing the sample vapor to escape the oven through a long 0.3 mm-diameter stainless steel capillary. The resulting molecular beam was directed to intersect with the electron beam inside the anion fragment mass-spectrometer. Anions were extracted with a 4π angular acceptance by a repeller electrode that was pulsed using a common trigger from the electron gun and a variable delay to accommodate the varying electron speed as a function of beam energy. The anion time-of-flight through the spectrometer depends on its mass-to-charge (m/z) ratio. Single anion hits were detected by an 80 mm MCP detector, allowing anions of differing masses to be distinguished clearly from each other, within a typical resolution of $m/\Delta m < 30$.

RESULTS

A. Photoelectron yield

Photoelectron spectra of six different gas-phase samples are shown in figure 1 (corresponding raw and inverted images are shown in Fig. S2). The spectra are obtained after ionization of the molecules by 13.5 nm EUV radiation and are shown in terms of kinetic energy of the emitted electrons. At the high kinetic energy (corresponding to the low electron binding energy) all photoelectron spectra demonstrate a wide peak due to emission of valence electrons. For high kinetic energy electrons, the widths of the valence peak features are limited by the mediocre energy resolution of the VMI photoelectron spectrometer.

To facilitate the assignment of the spectral features, a simple model was used to simulate photoelectron spectra, which are plotted on top of the experimental data in red (Fig. 1). The positions of the model spectrum peaks correspond to calculated atomic line energies found in ref. 21, whereas the intensities of the peaks are proportional to the atomic photoionization cross-sections, taken either from the same publication[21] or from the experimental work[22] for bromine and iodine, because of significant difference in the cross-section values for these two elements. Due to its simplicity the model is presented here only to guide the assignment of the peaks in the experimental photoelectron spectra. Thus, the model does not account for the shift of the peak positions and for the broadening of the sharp atomic lines in the valence band of the investigated molecular systems, which is observed in the experimental data. The model spectra are convoluted with a Gaussian function with FWHM of 2 eV to compare with the experimental line shapes.

From analysis of the model spectra it becomes obvious, that the broad peak in the experimental data is comprised of the H, C, and O valence bands. For the halogenated molecules, a valence peak of the corresponding halogen also appears in the valence band. For Cl-MPh, Br-MPh, and I-MPh, cross-sections of the halogen *s* or *p* electrons are small or negligible and do not affect the intensity of the valence peak (Fig. 1c,d,e). In contrast, fluorine has a 2*p* energy level with a binding energy around 17 eV, which has a substantial photoionization cross-section at 13.5 nm; its influence is clearly observed in the model spectrum of F-MPh and in the increased intensity of the valence peak in the experimental data (Fig. 1b). The role of the increased fluorine photoionization cross-section is even more pronounced in the valence band of 2,3,5,6-tetrafluoro-4-(trifluoromethyl)phenol due to the presence of seven fluorine atoms per molecule. The fluorine 2*s* energy level, despite its lower photoionization cross-section is also observed in the experimental data around 52 eV kinetic energy (Fig. 1f).

Br-MPh and I-MPh have core electron levels in addition to the valence band, which can be ionized by EUV radiation. For Br-MPh, a Br 3*d* peak is observed at a kinetic energy of 16.0 eV, corresponding to a binding energy of 76.0 eV, whereas the corresponding model peak is found at a lower kinetic energy of 11.4 eV (Fig. 1d). The binding energy of 76.0 eV is consistent with a literature value of 76.7 eV for CH_3Br though,[23] which is assumed to be a better model system for Br-MPh as compared to atomic bromine.

For I-MPh a sharp feature around 35.2 eV kinetic energy is due to the iodine 4*d* energy level (Fig. 1e). The experimental peak is split into two close lying peaks at 34.4 eV and 35.9 eV due to spin-orbit splitting into the corresponding $4d_{3/2}$ and $4d_{5/2}$ components. The binding energy, corresponding to the position of $4d_{5/2}$ line is 56.1 eV and the spin-orbit splitting is 1.5 eV. For comparison, the $4d_{5/2}$ peak was found at 56.7 eV for CH_3I,[24] while the spin-orbit splitting is 1.7 eV for CH_3I and for atomic iodine.[25]

The broad feature observed in the experimental spectrum of I-MPh from 5 to 30 eV is not represented in the model. This feature emerges due to emission of an additional electron via an Auger process. This was proven by measuring the photoelectron spectrum at higher photon energy which led to an increase in the photoelectron kinetic energy but did not change the Auger electron kinetic energy (Fig. S3). The NVV Auger electron spectrum of HI was observed in the kinetic energy region 25 to 30 eV,[26,27] alkali iodide molecules emitted Auger electrons in a similar energy range.[28] This process can correspond to the Auger peak observed in the experimental data at kinetic energies between 25-33 eV.

However, the iodo-methylphenol molecules have a broader valence band as observed here compared to HI and alkali iodide molecules. This could lead to other transitions which could explain appearance of an additional peak at kinetic energies between 10-20 eV. An Auger peak for HBr was observed[29] at kinetic energy around 40-46 eV and is not observed in the photoelectron spectrum of Br-MPh, Fig. 1d. This could be due to low absorption of EUV photons by Br level, validated by the low Br 3*d* peak intensity, which will lead to even lower probability of the Auger process.

An excited electronic system can relax not only by emitting an electron, but also through fluorescence. The fluorescence yield for the light chemical elements is negligible in comparison to electron emission, but it becomes more important with increasing atomic number. Nevertheless, the fluorescence yield is less than 1% for the M and N electron shells in bromine and iodine,[30] and therefore can be neglected in the present study.

The area of the photoelectron spectra normalized to the molecule number density and to the photon flux (determined as described in the Experimental methods section) is presented by the gray columns in Figure 2. After normalization, the height of the columns is proportional to the number of electrons emitted by a single molecule after being illuminated by a single EUV photon. It is instructive to see that the number of electrons emitted by I-MPh is about 1.6 times larger than that of 2,3,5,6-tetrafluoro-4-(trifluoromethyl)phenol, and 4 to 11 times larger than that of the remaining molecules. To understand the observed difference, we compare the experimental results with a model, which is proportional to the photoionization cross-sections, found as a sum of atomic cross-sections[22] of the corresponding molecules, and is shown in Fig. 2 by solid red columns. The good correlation between the model and the experiment is observed for all molecules, excluding I-MPh, and suggests that the number of emitted electrons is primarily determined by the photoabsorption properties of the molecules. The model predicts emission of the same number of electrons by I-MPH and 2,3,5,6-tetrafluoro-4-(trifluoromethyl)phenol although the experiment demonstrates emission of ~63% more electrons by I-MPh. This discrepancy is due to the contribution of Auger electrons which is not accounted for by the model.

The model can be expanded to account for the Auger electrons, assuming that each photon absorbed by a core electronic level will lead to emission of a photoelectron followed by emission of the Auger electron. For I-MPh 77% and for Br-MPh 22% of the total absorption cross-section is due to core level absorption. This is shown in Fig. 2 by a dashed red column on top of a solid column, accounting for emission of primary photoelectrons. This modified model accounts for the number of emitted electrons observed in the experiment and additionally confirms that a single I-MPh molecule emits ~63% more electrons than predicted by the simple model, based on the photoabsorption cross-sections of corresponding chemical elements, due to Auger decay.

Although most of the investigated molecules differ only by a single atom substitution, such a simple substitution can lead to extremely different properties: a) Substitution of a single MPh hydrogen atom by an iodine atom will lead to 4.6-fold increase of EUV photoabsorption cross-section. b) I-MPh and 2,3,5,6-tetrafluoro-4-(trifluoromethyl)phenol, despite their comparable photoabsorption properties demonstrate different electron yield due to emission of Auger electrons by I-MPh molecule. c) These two molecules also emit most of electrons with remarkably different kinetic energies. I-MPh emits electrons with kinetic energies mostly below 40 eV, whereas electrons emitted by 2,3,5,6-tetrafluoro-4-(trifluoromethyl)phenol have kinetic energy above 40 eV. These properties can be used for a predictive design of efficient EUV resists.

B. Molecular fragmentation after photoionization

To understand what happens to an isolated gas-phase molecule after absorption of an EUV photon and emission of an electron (the processes described above) a mass-spectrometry experiment was conducted. All mass-spectra are presented in Fig. S4 of the supplementary information; Br-MPh will be reported here as an example. Its mass-spectrum from photoionization with 13.5 nm (92 eV) photons is shown in Fig. 3a. Due to the limited mass resolution of VMI apparatus (see Experimental Methods section), the spectrum has low signal-to-noise ratio and the mass peaks are noticeably broad.

To assist with assignment of the peaks in the EUV mass-spectra, an additional experiment with vacuum ultraviolet ionization of gas-phase molecules was performed with much better mass resolution (Fig. 3b). The mass-spectrum of Br-MPh measured at the photon energy of 15 eV has a number of prominent peaks (Fig. 3b). Some of them can be easily assigned as a water molecule (m/z 18), oxygen (m/z 32), and the parent Br-MPh molecule cation, with peaks at m/z 186 and 188 (due to ^{79}Br and ^{81}Br isotopes, which have almost identical abundance, with ^{79}Br being slightly more abundant). Appearance of a single peak at m/z 107 can be explained by the dissociation of the Br-MPh molecule via elimination of a neutral bromine atom (defined as Hal in the equation below):

$$\text{Hal-}C_7H_7O^+ \rightarrow C_7H_7O^+ + \text{Hal} \rightarrow C_7H_5^+ + H_2O + \text{Hal} \qquad (1)$$

A similar dissociation pathway was previously observed for Cl-MPh, where photoionization of a parent molecule led to appearance of the $C_7H_7O^+$ (m/z 107) fragment.[31] Smaller fragments observed in the Br-MPh mass-spectrum in Fig. 3b were also detected in previous studies of fragmentation of methylphenols (C_7H_8O).[32–34] The cation $C_7H_7O^+$ (m/z 107) can fragment eliminating CO to $C_6H_7^+$ (m/z 79) and further elimination of H_2 will lead to appearance of $C_6H_5^+$ (m/z 77), both observed in the experimental mass-spectra:

$$C_7H_8O^+ \rightarrow C_7H_7O^+ + H \rightarrow C_6H_7^+ + CO + H \rightarrow C_6H_5^+ + H_2 + CO + H \qquad (2)$$

Branching ratios of these two fragments, $C_6H_7^+$ and $C_6H_5^+$ was found to be precursor molecule specific,[32] what is also observed in the present study in Fig. S5.

There is similarity in fragmentation of methylphenol and halogenated-methylphenols (see Fig. S5), but with one exception. While fragmentation of halogenated methylphenols leads to appearance of m/z 89, the corresponding peak is not observed in the mass-spectrum of methylphenol. Instead a peak at m/z 90 is observed. Appearance of the peak can be explained by the fragmentation of ionized methylphenol via elimination of a neutral water molecule, leading to appearance of $C_7H_6^+$ (m/z 90):

$$C_7H_8O^+ \rightarrow C_7H_6^+ + H_2O \qquad (3)$$

For halogenated methylphenols, the neutral water molecule can be eliminated from $C_7H_7O^+$ cation and cause appearance of m/z 89 ($C_7H_5^+$) peak in accordance with reaction (1), which is observed in the experimental data (Fig. 3b). In the case of expulsion of neutral water from the Hal-MPh cation similar to process (3), the fragmentation will lead to appearance of Hal-C_7H_5 cation:

$$\text{Hal-}C_7H_7O^+ \rightarrow \text{Hal-}C_7H_5^+ + H_2O \tag{4}$$

Traces of Br-C_7H_5 cation are observed in the mass-spectrum (Fig. 3b) as peaks with m/z 168 and 170.

In the mass-spectrum of MPh, a peak m/z 80 ($C_6H_8^+$) is observed that had been reported earlier too.[32] In that study, it was observed that the intensity of the peak is photon energy dependent, with the intensity of m/z 80 decreasing with increase of photon energy. The $C_6H_8^+$ fragments further to $C_6H_7^+$ (m/z 79) by eliminating an H atom:

$$C_7H_8O^+ \rightarrow C_6H_8^+ + CO \rightarrow C_6H_7^+ + H + CO \tag{5}$$

Using the ability of the synchrotron light source to tune photon energy, additional information can be obtained. Photoionization efficiency (PIE) curves can be obtained by collecting mass-spectra at different photon energies and presenting intensities of particular mass peaks as functions of photon energy. A PIE curve of Br-MPh is presented in Fig. 4a, whereas PIE curves of MPh, Cl-MPh, and I-MPh are shown in the Supplementary Information (Fig. S6). Onsets of a particular PIE curve can reveal information on ionization or fragmentation processes. The onset of the PIE curve of the parent molecule, Br-$C_7H_7O^+$ at 8.15 eV corresponds to the ionization energy (IE) of the molecule. Further increase of the photon energy leads to a rise of the parent cation yield until an appearance energy (AE) of 11.10 eV is reached, at which an additional peak m/z 107, corresponding to fragment $C_7H_7O^+$, appears via a fragmentation process (1). Comparison of the two values (IE and AE), leads to a conclusion that around 3 eV of extra energy above the ionization energy is needed to fragment the parent molecule cation. Deposition of even more energy into a molecule will lead to observation of additional fragmentation channels. Absorption of photons with energies above 11.80 eV leads to the appearance of $C_6H_7^+$ (m/z 79). Starting from photon energy of 13.50 eV, the $C_6H_5^+$ (m/z 77) fragment can be detected.

C. Interaction of electrons with neutral molecules

Inelastic collisions of electrons emitted as a result of photoionization and Auger processes with the neutral resist molecules in condensed phase resist material can lead to additional fragmentation channels. This process can be investigated by probing the fragmentation of gas-phase resist molecules in electron impact ionization. Similarly to photoionization process, the mass-spectra of cationic species were collected. The Br-MPh 53 eV electron impact ionization mass-spectrum is shown in Fig. 3c. The spectrum has a set of well resolved peaks, some of which have the same m/z as observed in the VUV photoionization mass-spectrum in Fig. 3b. Apart from the two parent peaks, peaks with m/z 107, 89, and 77 are present in both mass-spectra. But in the case of electron ionization, additional smaller fragments are observed, such as m/z 27, 39, 51, and 63, these peaks were also observed in the resonant enhanced multiphoton ionization (REMPI) mass-spectra of *p*-cresol (4-methylphenol).[33] Although the peaks were ing assigned in the REMPI study, these masses may correspond to chemical formulae C_2H_3, C_3H_3, C_4H_3, and C_5H_3 for m/z 27, 39, 51, and 63, correspondingly. The appearance of additional fragment peaks may be rationalized by deposition of extra energy (53 eV vs. 15 eV) into the parent molecule in the process of inelastic electron collision comparing with VUV photoionization, leading to more intense fragmentation. A comparison of the e-beam (Fig. 3c) and the EUV mass-spectra (Fig. 3a) reveals similarities. This comparison is shown in Supplementary information Fig. S8. Analyzing the overlaid spectra demonstrates that most of the fragments have the same masses and even similar abundances.

The mass-spectra can be collected during electron impact ionization with different kinetic energies, in a manner similar to the collection of PIE curves during VUV photoionization. The dependence of mass peak intensities vs. electron kinetic energy will provide information similar to that found in the PIE curves. In the case of electron ionization, the electron ionization efficiency (EIE) curves can also assist in measuring appearance energies of fragments. The EIE curves for Br-MPh are shown in Fig. 4b. The appearance energies of fragments for both photon and electron ionization processes are summarized in Table S2, whereas all EIE spectra are shown in Fig. S9. The obtained results suggest, that similarly to the photoionization case, interaction of a neutral molecule with an energetic electron (kinetic energy > 20 eV) will lead to its fragmentation via a number of possible fragmentation channels. The fragmentation reactions are directly related to the processes occurring in a resist film after the EUV exposure. Electrons, generated during the exposure, will interact with polymer (monomers of which are studied in gas-phase) and lead to its fragmentation, causing the solubility change of the resist material, one of the key steps of photolithography process.

D. Dissociative electron attachment

Low energy electron interactions with molecules are resonantly enhanced by metastable electronic states, which are compound electron-molecule systems, temporarily stabilized by the interaction between the incident electron and the electrons of the target molecule.[35,36] These transient anion states can initially decay by electron autodetachment. At the same time, a transient anion may also perform isomerization or dissociation, in competition with autodetachment, to electronically stabilize the system and prevent the additional electron from detaching. Resonances will enhance ionization and dissociation processes, and one important class of these processes, dissociative electron attachment (DEA), occurs exclusively below the first electronically excited state of a molecular system. DEA is a resonant collision between a low-energy electron and a molecule, resulting in a transient anion that subsequently dissociates.

DEA to I-MPh produces three anion fragments, with strong dependence on electron energy, as shown in Fig. 5. The dominant fragments are I^- (m/z 127) and $C_7H_7O^-$ (m/z 107), which can both be produced by C-I bond scission. The two anion fragments are produced in two resonances near incident electron energies of 4.5 eV and 8 eV, with the I^- yield being higher by a factor of about 3 in each of these resonances. I^- was also detected at resonances around 1.5 eV and 5.5 eV, the latter bring a high energy shoulder on the 4.5 eV resonance feature (Fig. 5c).

The results for the HNIT molecule are shown in Fig. S10. This system is dominated by at least three broad resonance structures, spanning from 1 eV to 10 eV, producing a triflate anion $CF_3SO_3^-$ (m/z 149), with a peak yield near 3 eV incident electron energy, and resonance features apparent as high energy shoulders near 5 eV and 7 eV. Triflyl anions, $CF_3SO_2^-$ (m/z 133) are also produced with a qualitatively similar energy dependence, suggesting competing dissociation pathways involving N-O or S-O bond scission. The complementary anion fragments $C_{12}H_6NO_2^-$ (m/z 196) and $C_{12}H_6NO_3^-$ (m/z 212) were also detected with a yield less than 0.05 relative to the yield of triflate anions. A direct comparison can be drawn between these N-O and S-O bond breaking channels and the C-O and S-O bond breaking channels reported by Ptasinska *et al.*[15] for methyl triflate, phenyl triflate and tolyl triflate. Below 4 eV, the low energy structures in the fragment yields of the present data for HNIT are comparable with methyl triflate. For the latter target, Ptasinska *et al.* reported a 1 eV threshold and higher relative yield for the triflyl anion, and a 0 eV threshold for the triflate anion, in contrast to phenyl triflate and tolyl triflate, which each exhibited similar energetic thresholds and similar yields for the same two anion fragments. In the present data, the triflyl anion is produced with a sharp onset energy of about 1 eV, peaked at 2.5 eV, while the triflate anion has a broader onset peaked at about 3 eV and approximately 5-fold higher yield. HNIT also produces significant yields of each of the two anions resulting from simple N-O bond break at higher energies up to 8 eV. In contrast to phenyl triflate and tolyl triflate[15], no SO_2F^- was observed for HNIT in the present experiments, however a significant relative yield of OCF_3 was observed, with a similar incident electron energy dependence to the anions produced by S-O bond break, suggesting intramolecular rearrangement in the transient HNIT anion.

E. Outlook: From gas-phase molecules to condensed resist

The transition from an isolated gas-phase molecule to the condensed resist material will change some of the material properties: electron energy levels will broaden into energy bands which may also slightly shift in energy, but the energies of emitted electrons can still be studied using the gas-phase photoelectron spectroscopy technique described above. In this case, instead of using a beam of gas-phase resist molecules or effusive source of molecules, an aerosol method of preparing EUV resist material nanoparticles can be incorporated into the spectrometer. These nanoparticles (100-500 nm in diameter) can be synthesized using different techniques and the nanoparticles can have various morphologies. The nanoparticles could be homogeneous (Fig. 6a, left), they may have a core-shell structure, with a EUV inactive core (SiO_2 for example, emulating the silicon wafer) covered by a resist material (Fig. 6a, center), or they may even have (sub)nanometer-sized metal inclusions enhancing absorption of EUV photons (Fig. 6a, right).

As a demonstration of the technique, PMMA nanoparticles were generated, aerosolizing 1 wt% solution of PMMA in anisole. Aerosolized droplets of the solution can be transported inside of metal tubing in flowing non-reactive gas, such as nitrogen, without deposition of nanoparticles. During the transportation, the droplets will eventually evaporate the solvent and generate solid PMMA nanoparticles. The size distribution of these generated nanoparticles was measured using a scanning mobility particle sizer and is shown in Fig. 6b. It is apparent that most of the unsupported nanoparticles have diameter from 100 to 200 nm, whereas the whole size distribution ranges from approximately 50 to 600 nm. A set of aerodynamic lenses[37–39] allows for focusing of the beam of unsupported nanoparticles into a vacuum apparatus. This beam is directed in the interaction region of the VMI photoelectron spectrometer, where it is intersected by an EUV radiation beam. The kinetic energies of the electrons emitted as a result of EUV photoabsorption are detected by the VMI photoelectron spectrometer. The photoelectron spectrum of the PMMA nanoparticles is shown in Fig. 6c. The spectrum demonstrates features at low binding energies (10 - 50 eV), which can be assigned to the PMMA valence band.[40,41] Spectral features at high binding energies (above 70 eV) are due to background at the center of the VMI detector (see Fig. S11).

Comparison of the photoelectron spectra of the gas-phase molecules to the spectra of their nanoparticles aggregates could demonstrate how the condensation of resist molecules changes the energy of emitted electrons. Resist condensation will lead to the kinetic energy loss of the emitted photo electrons via interaction with surrounding molecules. This process, called thermalization, can redistribute the energies of emitted electrons to the thermal energy of the resist material. Throughout thermalization, the inelastic scattering of electrons may also lead to emission of additional, secondary electrons.

Condensation of resist molecules may also change the fragmentation patterns, observed for the isolated gas-phase molecules. In the case of a condensed phase resist, the molecules and their fragments have limited range of motion because they are trapped in the resist film and because of this, fragments can recombine or generate secondary chemical reactions. These processes can still be studied using the approach described above. Molecules desorbed from the resist film can be detected using mass-spectrometry. Traditionally the measurement is performed using electron-impact ionization and quadrupole mass-spectrometers.[42–44] When compared to a planar film, resist nanoparticles bring the advantage of a much larger surface to volume ratio, leading to enhanced photon induced desorption of resist molecule fragments from their surface. An additional source of ionization will be needed to ionize desorbed neutral molecules or fragments in our apparatus.

CONCLUSIONS

The work demonstrates a comprehensive experimental characterization of gas-phase monomer units of a phenolic EUV resist material. The processes of photoabsorption, electron emission, and molecular fragmentation, directly related to the processes occurring in a photoresist film after EUV photon absorption, were studied using gas-phase photoelectron spectroscopy and mass-spectrometry techniques. In model phenolic resist molecules, halogen substituents may dramatically increase the photoabsorption of the molecule and the electron yield per absorbed EUV photon. It was demonstrated that iodo-methylphenol molecule may emit two electrons (one photo-electron and one Auger electron) after EUV photon absorption. The molecule also has a high EUV photoabsorption cross-section, significantly higher than the other molecules studied here. The fragmentation pattern of neutral gas-phase molecules, interacting with an electron beam was studied and observed to be similar to EUV photon fragmentation. Different fragmentation channels were discussed. The importance of low kinetic energy, thermalized electrons to EUV lithography was demonstrated by investigation of the dissociative electron attachment process. It was confirmed that low kinetic energy electrons led to formation of anion fragments due to resonant electron-molecule interactions. The research described here is then contextualized to provide a roadmap for EUV investigation of condensed resist molecules.

SUPPLEMENTARY MATERIAL

See Supplementary Material for tables of molecular number densities used in the study and appearance energies after photo- and electron-impact ionization, NEXAFS spectra, mass-spectra detected using EUV, VUV, and electron-impact ionization, photo- and electron-impact ionization efficiency curves of studied materials, anion fragment yields due to dissociative electron attachment to N-Hydroxynaphthalimide triflate.

ACKNOWLEDGEMENTS

This work, the Advanced Light Source and the Molecular Foundry are supported by the Director, Office of Science, Office of Basic Energy Sciences, and by the Division of Chemical Sciences, Geosciences and Biosciences, of the U.S. Department of Energy under Contract No. DE-AC02-05CH11231. M. A. and O.K. were supported by the Gas Phase Chemical Physics Program under the same DOE contract. B.X., K.D.C., and partially O.K. were supported by the Laboratory Directed Research and Development (LDRD) Program at LBNL, also supported under the same DOE contract.

CITATIONS

[1] G.L.T. Chiu and J.M. Shaw, IBM J. Res. Dev. **41**, 3 (1997).
[2] B.J. Lin, in *Opt. Microlithogr.* (International Society for Optics and Photonics, 1988), pp. 256–270.
[3] R.P. Seisyan, Tech. Phys. **56**, 1061 (2011).
[4] A. Pimpin and W. Srituravanich, Eng. J. **16**, 37 (2012).
[5] H. Kinoshita, T. Kaneko, H. Takei, N. Takeuchi, and S. Ishihara, in (1986), pp. 28-ZF-15.
[6] A.M. Hawryluk and L.G. Seppala, J. Vac. Sci. Technol. B Microelectron. Process. Phenom. **6**, 2162 (1988).
[7] A. Pirati, R. Peeters, D. Smith, S. Lok, M. van Noordenburg, R. van Es, E. Verhoeven, H. Meijer, A. Minnaert, J.-W. van der Horst, H. Meiling, J. Mallmann, C. Wagner, J. Stoeldraijer, G. Fisser, J. Finders, C. Zoldesi, U. Stamm, H. Boom, D. Brandt, D. Brown, I. Fomenkov, and M. Purvis, in *Extreme Ultrav. EUV Lithogr. VII* (International Society for Optics and Photonics, 2016), p. 97760A.
[8] B. Turkot, S.L. Carson, A. Lio, T. Liang, M. Phillips, B. McCool, E. Stenehjem, T. Crimmins, G. Zhang, and S. Sivakumar, in *Extreme Ultrav. EUV Lithogr. VII* (International Society for Optics and Photonics, 2016), p. 977602.
[9] R.A. Lawson and A.P.G. Robinson, in *Front. Nanosci.*, edited by A. Robinson and R. Lawson (Elsevier, 2016), pp. 1–90.
[10] S. Irie, M. Endo, M. Sasago, N. Kandaka, H. Kondo, and K. Murakami, Jpn. J. Appl. Phys. **41**, 4027 (2002).
[11] Y. Fukushima, T. Watanabe, T. Harada, and H. Kinoshita, J. Photopolym. Sci. Technol. **22**, 85 (2009).
[12] D.F. Ogletree, in *Front. Nanosci.*, edited by A. Robinson and R. Lawson (Elsevier, 2016), pp. 91–113.
[13] T. Kozawa and S. Tagawa, Jpn. J. Appl. Phys. **49**, 030001 (2010).
[14] K.D. Closser, D.F. Ogletree, P. Naulleau, and D. Prendergast, J. Chem. Phys. **146**, 164106 (2017).
[15] S. Ptasińska, D. Gschliesser, P. Bartl, I. Janik, P. Scheier, and S. Denifl, J. Chem. Phys. **135**, 214309 (2011).
[16] A.T.J.B. Eppink and D.H. Parker, Rev. Sci. Instrum. **68**, 3477 (1997).

[17] K.R. Wilson, S. Zou, J. Shu, E. Rühl, S.R. Leone, G.C. Schatz, and M. Ahmed, Nano Lett. **7**, 2014 (2007).
[18] O. Kostko, B. Xu, M.I. Jacobs, and M. Ahmed, J. Chem. Phys. **147**, 013931 (2017).
[19] R.I. Kaiser, P. Maksyutenko, C. Ennis, F. Zhang, X. Gu, S.P. Krishtal, A.M. Mebel, O. Kostko, and M. Ahmed, Faraday Discuss. **147**, 429 (2010).
[20] H. Adaniya, D.S. Slaughter, T. Osipov, T. Weber, and A. Belkacem, Rev. Sci. Instrum. **83**, 023106 (2012).
[21] J.J. Yeh and I. Lindau, At. Data Nucl. Data Tables **32**, 1 (1985).
[22] B.L. Henke, E.M. Gullikson, and J.C. Davis, At. Data Nucl. Data Tables **54**, 181 (1993).
[23] J. Johnson, J.N. Cutler, G.M. Bancroft, Y.F. Hu, and K.H. Tan, J. Phys. B At. Mol. Opt. Phys. **30**, 4899 (1997).
[24] J.N. Cutler, G.M. Bancroft, D.G. Sutherland, and K.H. Tan, Phys. Rev. Lett. **67**, 1531 (1991).
[25] J. Tremblay, M. Larzilliere, F. Combet-Farnoux, and P. Morin, Phys. Rev. A **38**, 3804 (1988).
[26] J.N. Cutler, G.M. Bancroft, and K.H. Tan, J. Phys. B At. Mol. Opt. Phys. **24**, 4987 (1991).
[27] L. Karlsson, S. Svensson, P. Baltzer, M. Carlsson-Gothe, M.P. Keane, A.N. de Brito, N. Correia, and B. Wannberg, J. Phys. B At. Mol. Opt. Phys. **22**, 3001 (1989).
[28] Z. Hu, A. Caló, E. Kukk, H. Aksela, and S. Aksela, Chem. Phys. **313**, 77 (2005).
[29] R. Püttner, Y.F. Hu, G.M. Bancroft, H. Aksela, E. Nõmmiste, J. Karvonen, A. Kivimäki, and S. Aksela, Phys. Rev. A **59**, 4438 (1999).
[30] J.H. Hubbell, P.N. Trehan, N. Singh, B. Chand, D. Mehta, M.L. Garg, R.R. Garg, S. Singh, and S. Puri, J. Phys. Chem. Ref. Data **23**, 339 (1994).
[31] C.J. Cassady, S. Afzaal, and B.S. Freiser, Org. Mass Spectrom. **29**, 30 (1994).
[32] D.H. Russell, B.S. Freiser, E.H. McBay, and D.C. Canada, Org. Mass Spectrom. **18**, 474 (1983).
[33] T.C. Chang and M.V. Johnston, J. Phys. Chem. **91**, 884 (1987).
[34] E.T.M. Selim, M.A. Fahmey, and H.S. Ghonime, Org. Mass Spectrom. **26**, 55 (1991).
[35] O. Ingólfsson, F. Weik, and E. Illenberger, Int. J. Mass Spectrom. Ion Process. **155**, 1 (1996).
[36] H. Hotop, M.-W. Ruf, M. Allan, and I.I. Fabrikant, in *Adv. At. Mol. Opt. Phys.*, edited by B. Bederson and H. Walther (Academic Press, 2003), pp. 85–216.
[37] P. Liu, P.J. Ziemann, D.B. Kittelson, and P.H. McMurry, Aerosol Sci. Technol. **22**, 293 (1995).
[38] X. Wang, F.E. Kruis, and P.H. McMurry, Aerosol Sci. Technol. **39**, 611 (2005).
[39] J. Shu, K.R. Wilson, M. Ahmed, and S.R. Leone, Rev. Sci. Instrum. **77**, 043106 (2006).
[40] E.A. Thomas and J.E. Fulghum, J. Vac. Sci. Technol. Vac. Surf. Films **16**, 1106 (1998).
[41] K. Endo, N. Kobayashi, M. Aida, and T. Hoshi, Polym. J. **28**, 901 (1996).
[42] K.R. Dean, I. Nishiyama, H. Oizumi, A. Keen, H. Cao, W. Yueh, T. Watanabe, P. Lacovig, L. Rumiz, G. Denbeaux, and J. Simon, in *Adv. Resist Mater. Process. Technol. XXIV* (International Society for Optics and Photonics, 2007), p. 65191P.
[43] E. Shiobara, Y. Kikuchi, S. Mikami, T. Sasami, T. Kamizono, S. Minegishi, T. Kimoto, T. Fujimori, T. Watanabe, T. Harada, H. Kinoshita, and S. Tanaka, in *Extreme Ultrav. EUV Lithogr. VII*, edited by E.M. Panning and K.A. Goldberg (International Society for Optics and Photonics, 2016), p. 97762H.
[44] P.M. Dentinger, J. Vac. Sci. Technol. B Microelectron. Nanometer Struct. Process. Meas. Phenom. **18**, 3364 (2000).

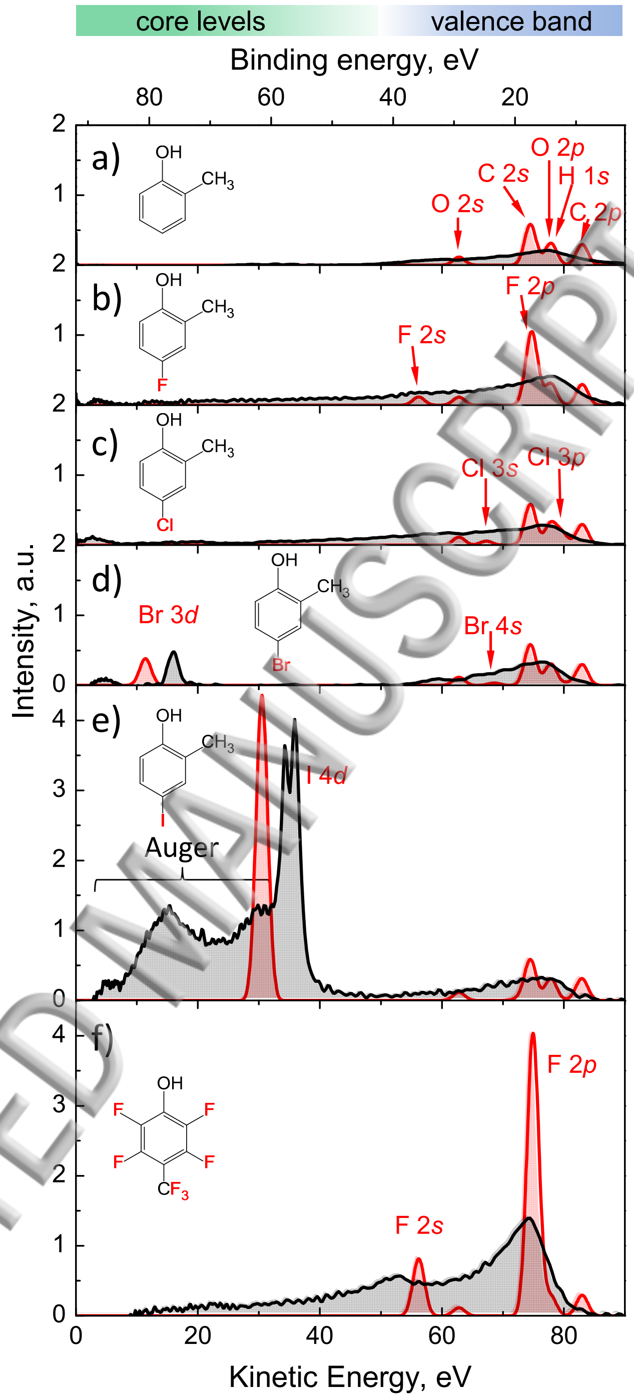

Figure 1. Photoelectron spectra of gas-phase molecules measured using 13.5 nm (92 eV) EUV radiation. Black line corresponds to experimental data, red line corresponds to model. a) 2-methylphenol, b) 4-fluoro-2-methylphenol, c) 4-chloro-2-methylphenol, d) 4-bromo-2-methylphenol, e) 4-iodo-2-methylphenol, f) 2,3,5,6-tetrafluoro-4-(trifluoromethyl)phenol. Different atomic energy levels of the model are labeled in red. Peaks labeled in panel a) are common for all presented spectra, therefore only new peaks corresponding to halogen atom(s) are labeled in panels b)-f).

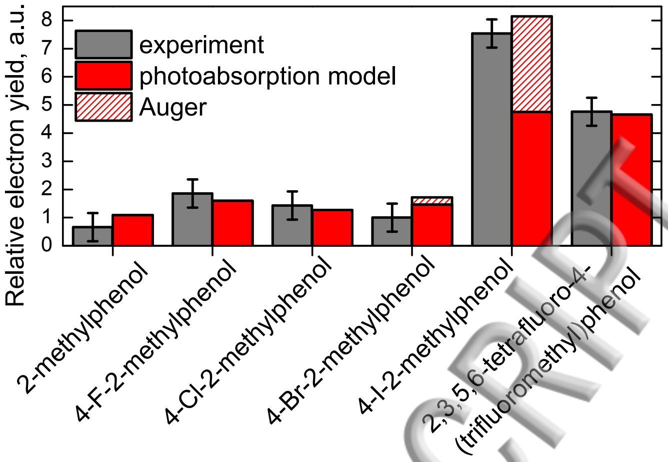

Figure 2. Relative electron yield for gas-phase phenolic molecules. Gray columns depict experimental electron yield and are normalized to unity for bromo-methylphenol. Red columns correspond to model electron yield.

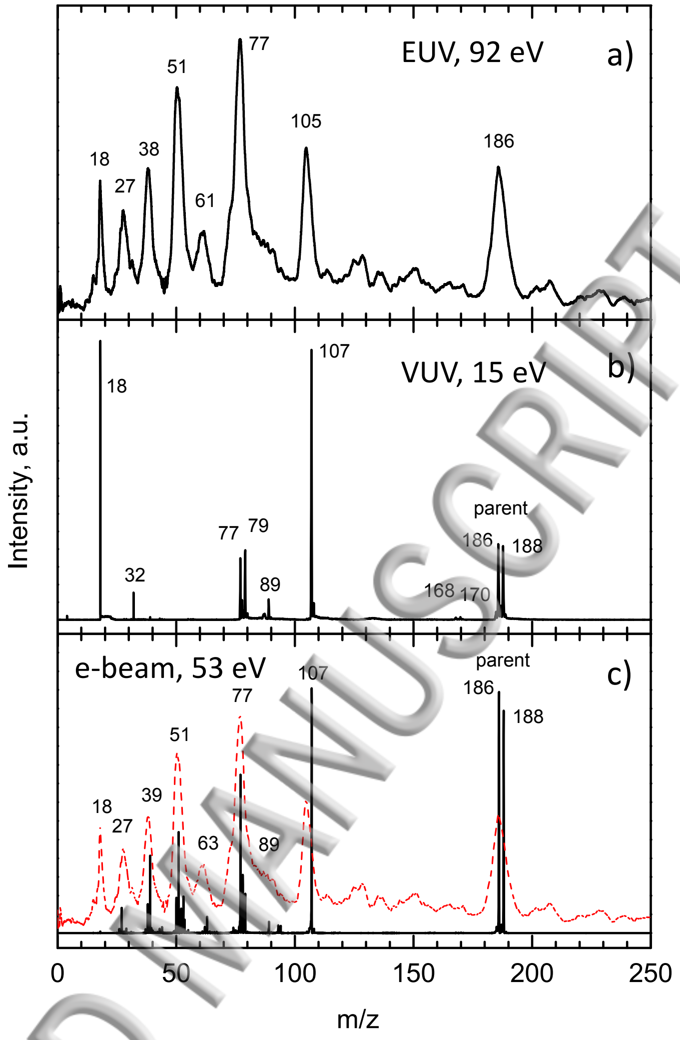

Figure 3. Mass-spectra of 4-bromo-2-methylphenol measured using: a) EUV radiation with photon energy 92 eV, b) VUV radiation with photon energy 15 eV, c) electron impact ionization with electron kinetic energy 53 eV. Red dashed line in panel c) corresponds to EUV mass-spectrum, shown in panel a) and shown here for comparison. Unlabeled signal in panel a) above m/z 110 is due to measurement noise that is also present with no gas sample.

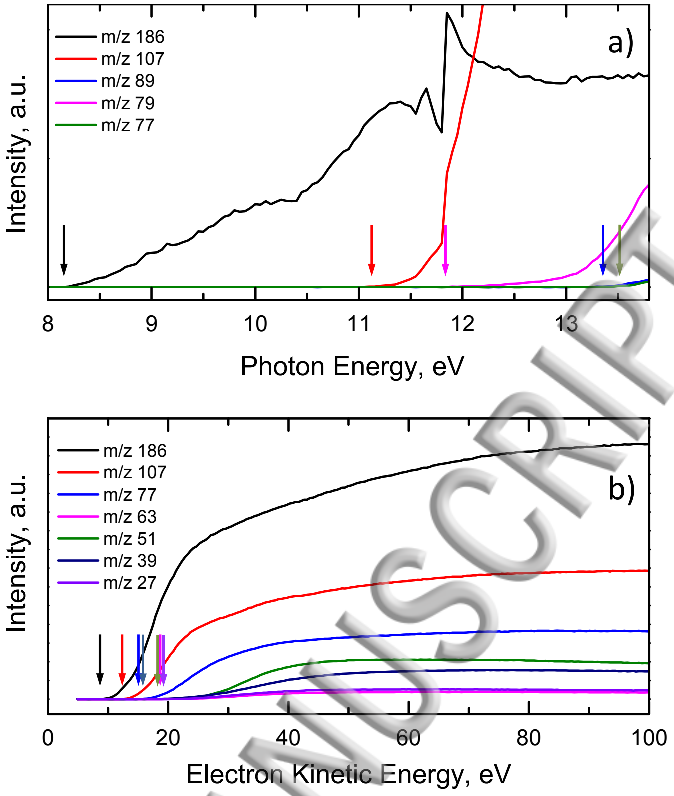

Figure 4. a) Photoionization efficiency curves for 4-bromo-2-methylphenol, measured using VUV radiation. b) Electron ionization efficiency curves, measured using electron gun as ionization source. Vertical arrows depict onsets of signal, corresponding to appearance energies. Discontinuity in the VUV PIE curve around 11.5-12.0 eV is due to absorption lines of argon used in a beamline’s gas filter (used to remove higher light harmonics, generated by an undulator).

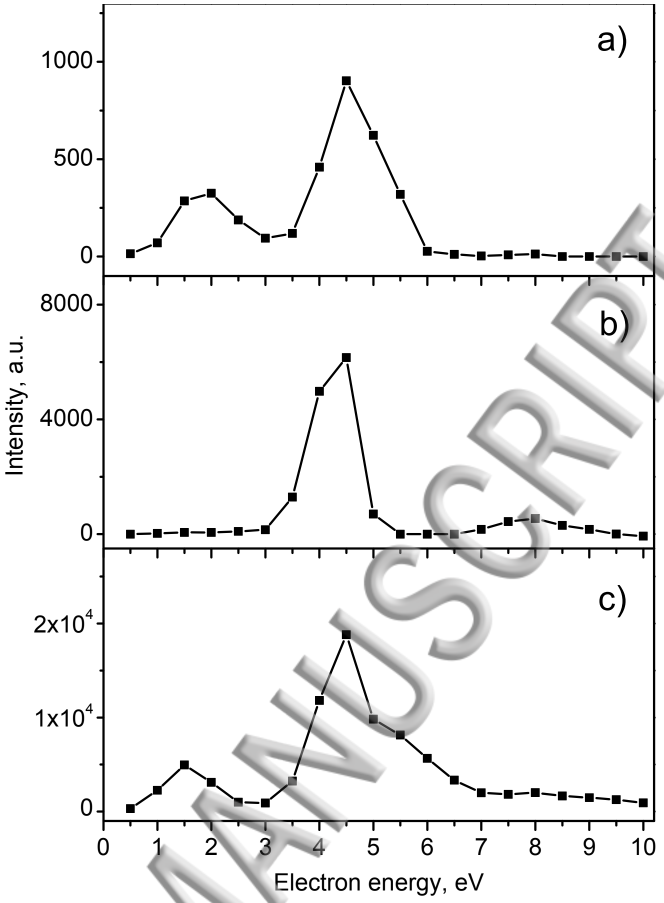

Figure 5. Yields of anion fragments produced by low energy electron impact to I-MPh: (a) I-MPh parent anion, (b) 2-methylphenol radical anion fragment ($C_7H_7O^-$), and (c) anion fragment I^-. A broad resonance feature near 4.5 eV produces both I^- and $C_7H_7O^-$ fragments. A smaller peak near 1.5 eV produces the I^- fragment exclusively. The parent anion $(I\text{-}MPh)^-$ was observed near the 4.5 eV resonance.

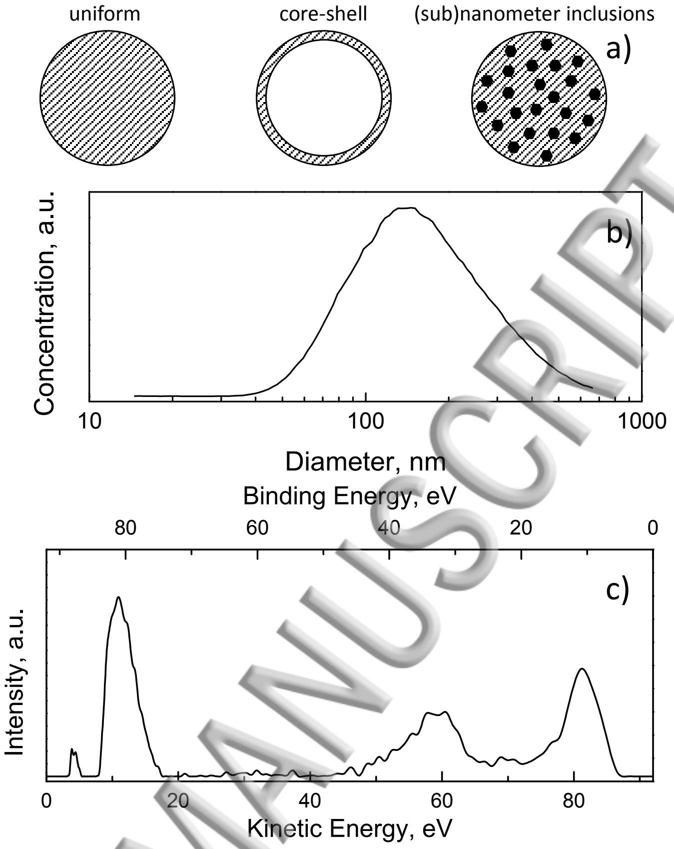

Figure 6. a) Different morphologies of nanoparticles. b) Size distribution of generated PMMA nanoparticles. c) Photoelectron spectrum of PMMA nanoparticles.

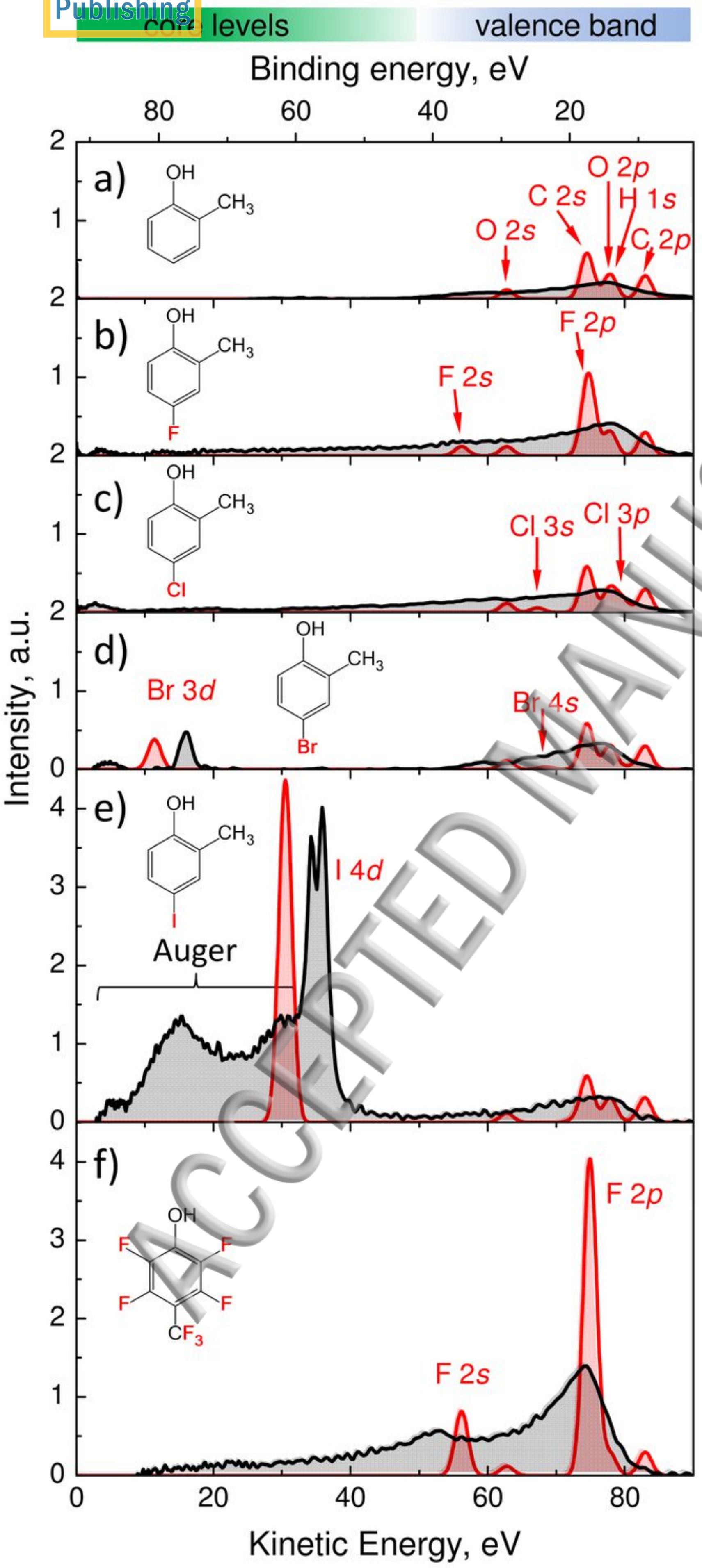
core levels
valence band
Binding energy, eV
80
60
40
20
a)
OH
CH3
O 2s
C 2s
O 2p
H 1s
C 2p
b)
F
F 2s
F 2p
c)
Cl
Cl 3s
Cl 3p
d)
Br 3d
Br
Br 4s
e)
I
I 4d
Auger
f)
F
CF3
F 2s
F 2p
Intensity, a.u.
0
1
2
3
4
Kinetic Energy, eV
0
20
40
60
80

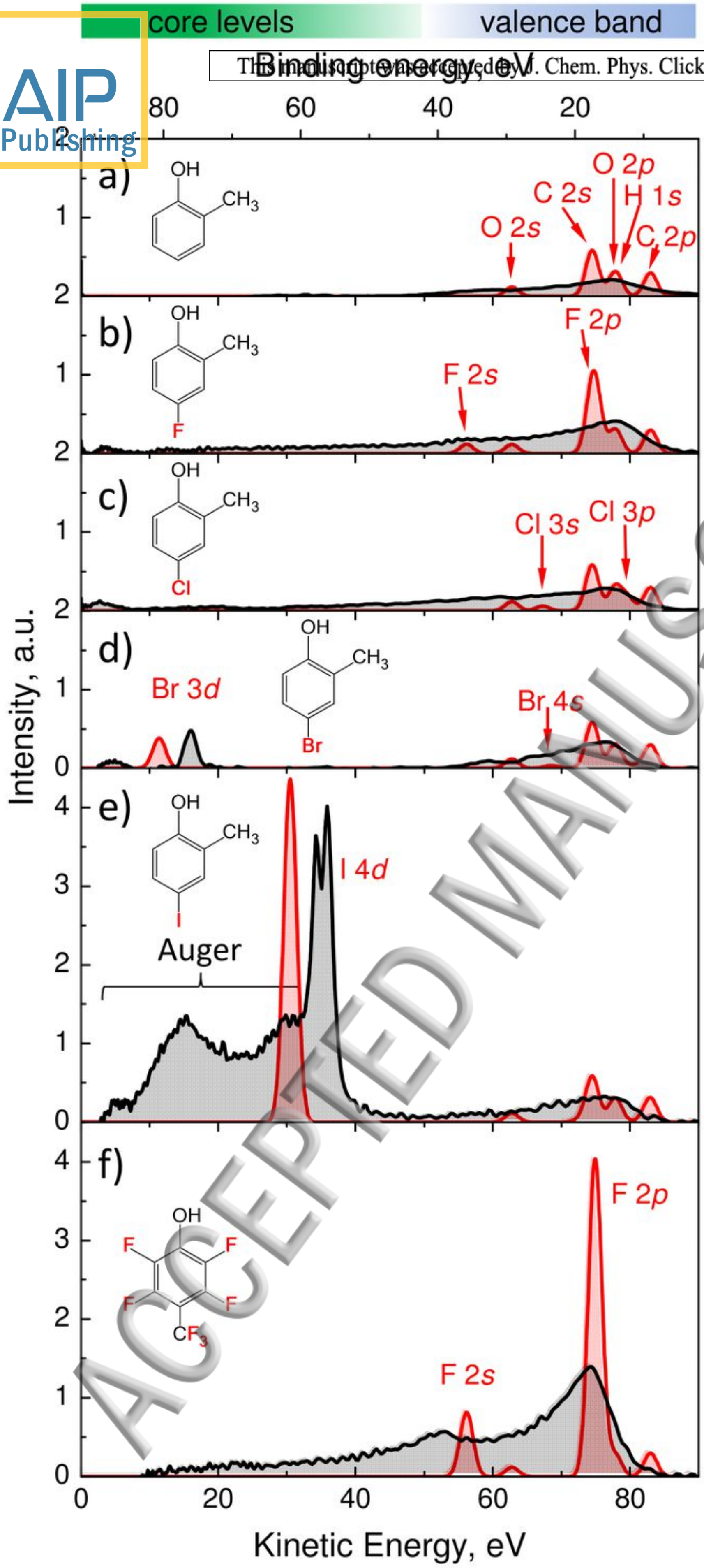
core levels
valence band
Binding energy, eV
80
60
40
20
a)
OH
CH$_3$
O 2p
C 2s
H 1s
O 2s
C 2p
b)
F 2p
F 2s
F
c)
Cl 3s
Cl 3p
Cl
d)
Br 3d
Br 4s
Br
e)
I 4d
I
Auger
f)
F
CF$_3$
F 2p
F 2s
Intensity, a.u.
0
1
2
3
4
0
20
40
60
80
Kinetic Energy, eV

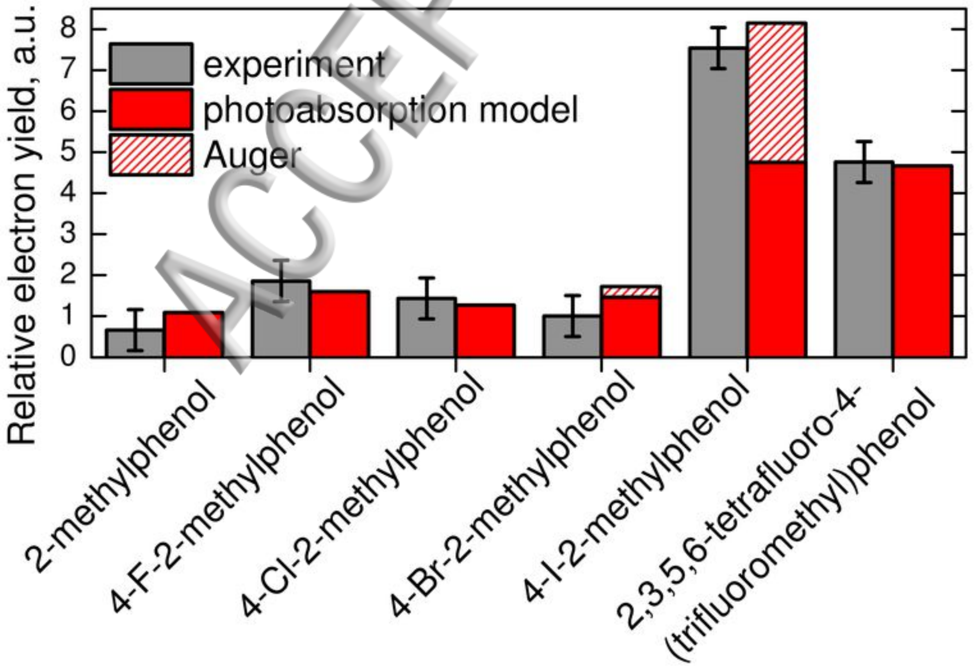
Relative electron yield, a.u.
0
1
2
3
4
5
6
7
8
experiment
photoabsorption model
Auger
2-methylphenol
4-F-2-methylphenol
4-Cl-2-methylphenol
4-Br-2-methylphenol
4-I-2-methylphenol
2,3,5,6-tetrafluoro-4-(trifluoromethyl)phenol

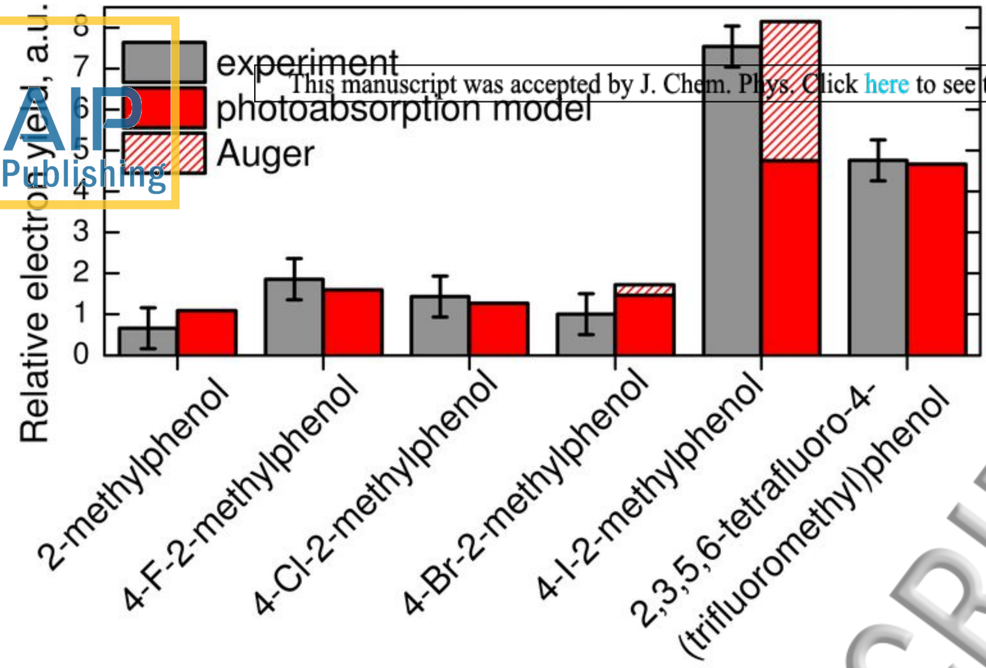
Relative electron yield, a.u.
0
1
2
3
4
5
6
7
8
experiment
photoabsorption model
Auger
2-methylphenol
4-F-2-methylphenol
4-Cl-2-methylphenol
4-Br-2-methylphenol
4-I-2-methylphenol
2,3,5,6-tetrafluoro-4-(trifluoromethyl)phenol

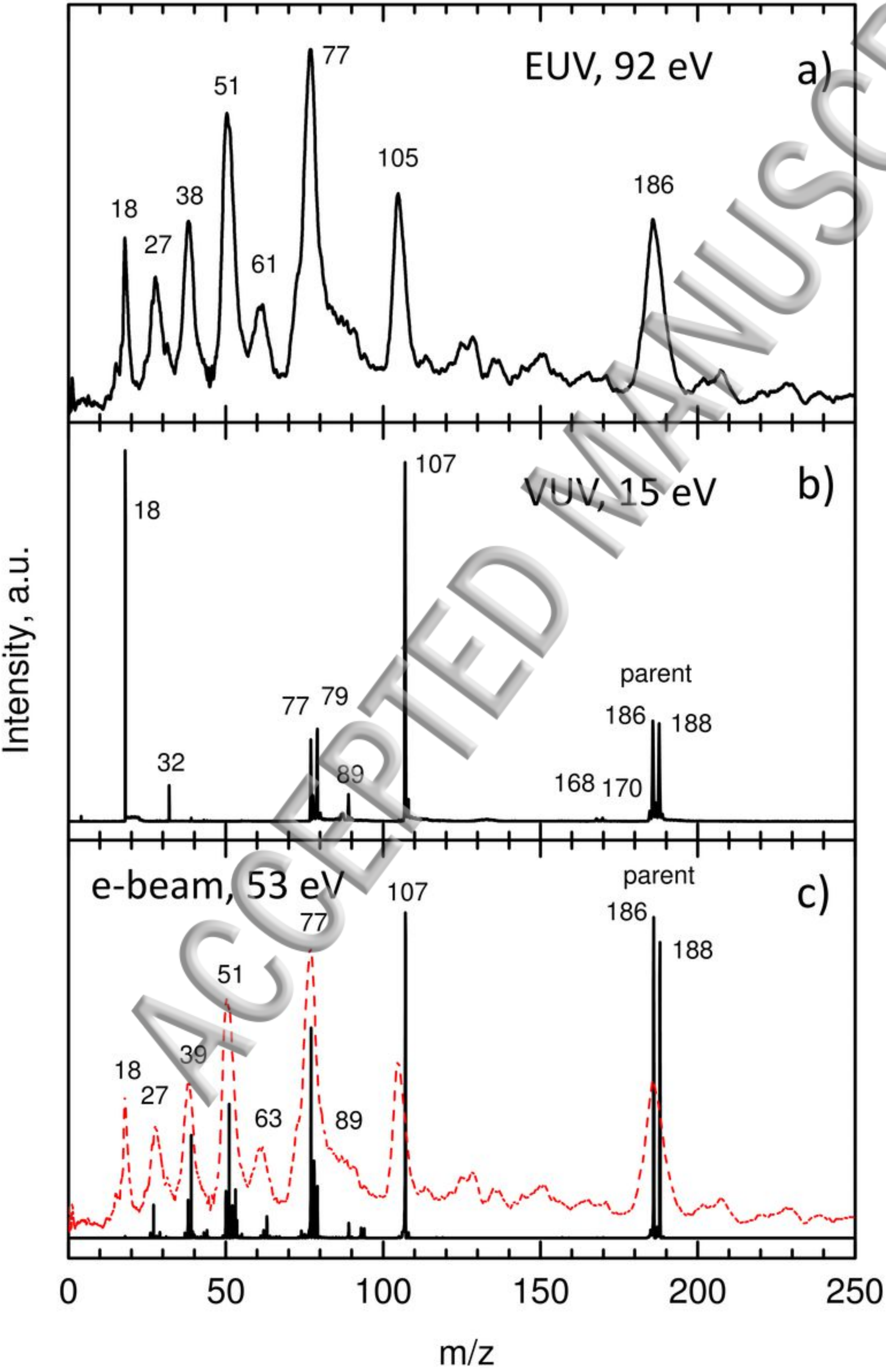
EUV, 92 eV
a)
18
27
38
51
61
77
105
186
VUV, 15 eV
b)
18
32
77
79
89
107
168
170
parent
186
188
e-beam, 53 eV
c)
18
27
39
51
63
77
89
107
parent
186
188
Intensity, a.u.
0
50
100
150
200
250
m/z

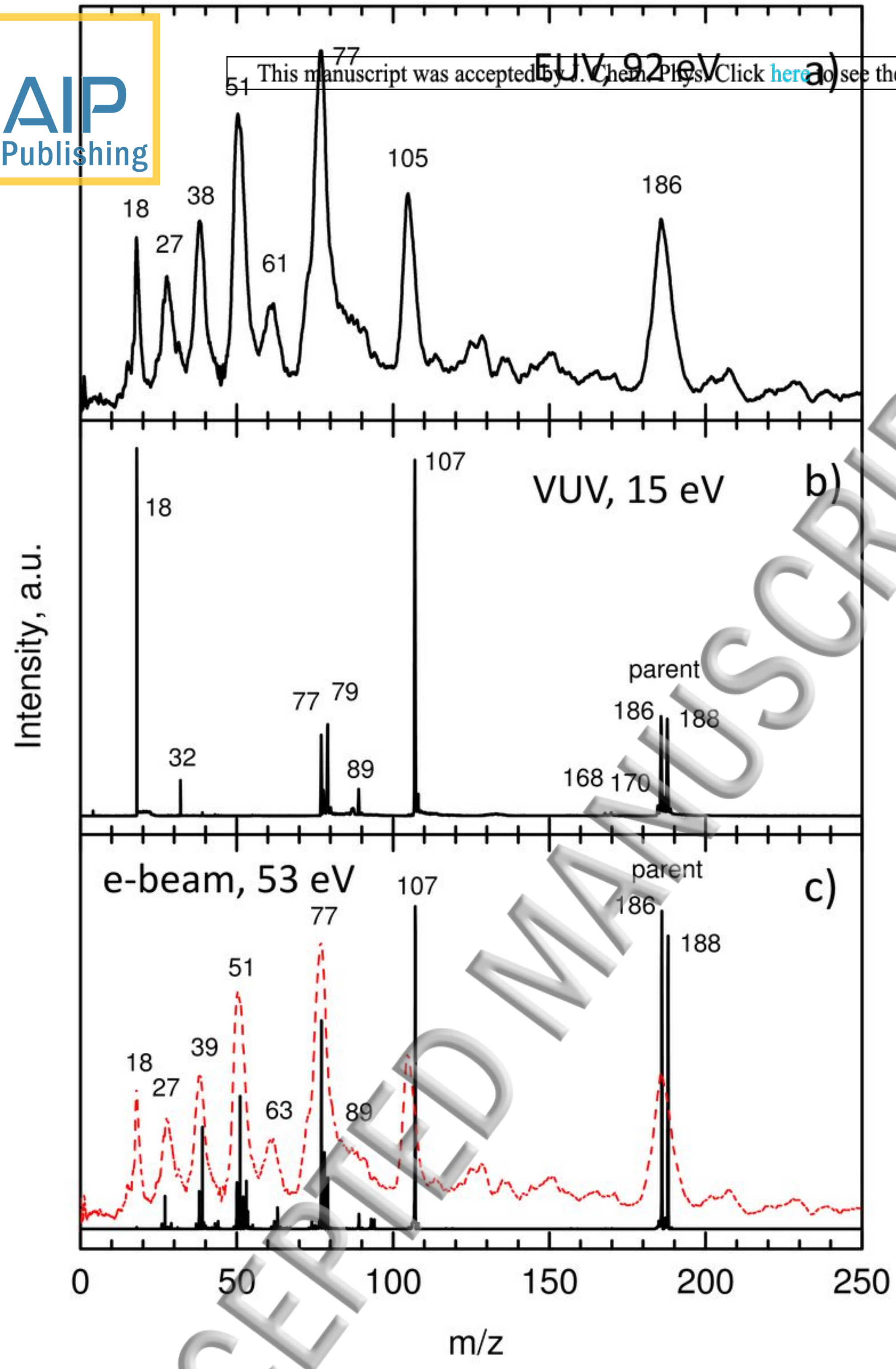
EUV, 92 eV
a)
18
27
38
51
61
77
105
186
VUV, 15 eV
b)
18
32
77
79
89
107
parent
186
188
168
170
e-beam, 53 eV
c)
18
27
39
51
63
77
89
107
parent
186
188
Intensity, a.u.
0
50
100
150
200
250
m/z

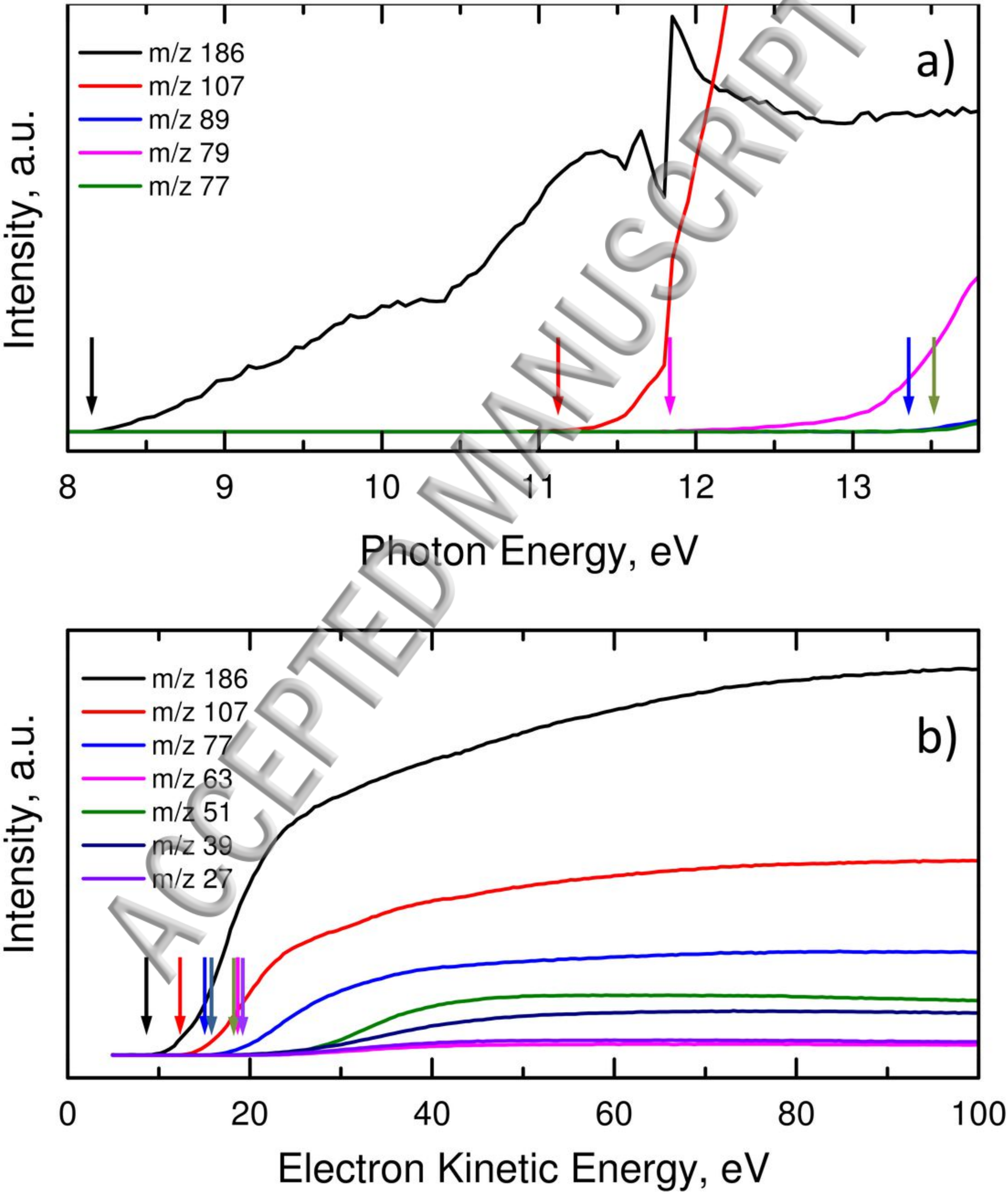
a)
m/z 186
m/z 107
m/z 89
m/z 79
m/z 77
Intensity, a.u.
8
9
10
11
12
13
Photon Energy, eV
b)
m/z 186
m/z 107
m/z 77
m/z 63
m/z 51
m/z 39
m/z 27
Intensity, a.u.
0
20
40
60
80
100
Electron Kinetic Energy, eV

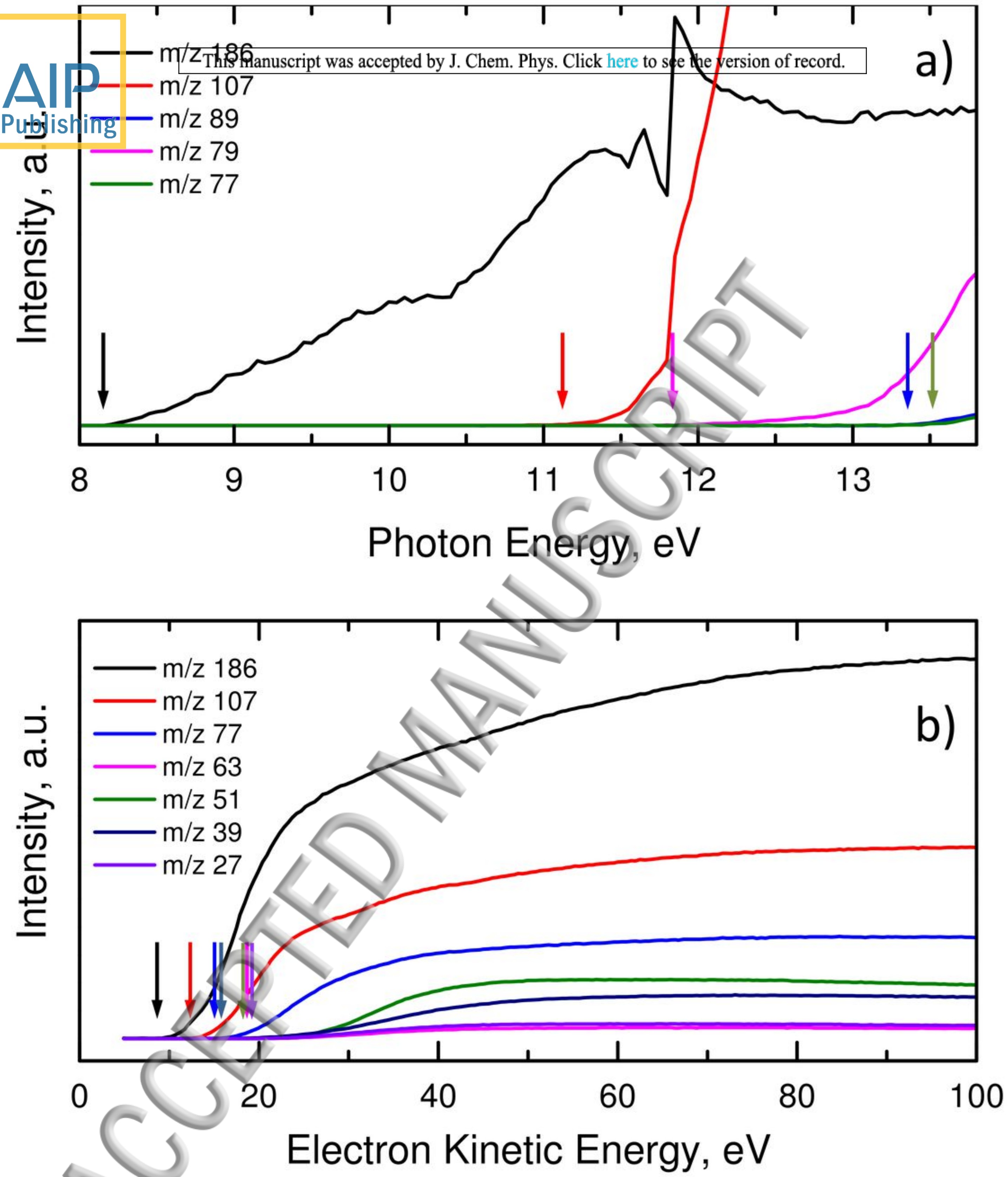
a)
m/z 186
m/z 107
m/z 89
m/z 79
m/z 77
Intensity, a.u.
8
9
10
11
12
13
Photon Energy, eV
b)
m/z 186
m/z 107
m/z 77
m/z 63
m/z 51
m/z 39
m/z 27
Intensity, a.u.
0
20
40
60
80
100
Electron Kinetic Energy, eV

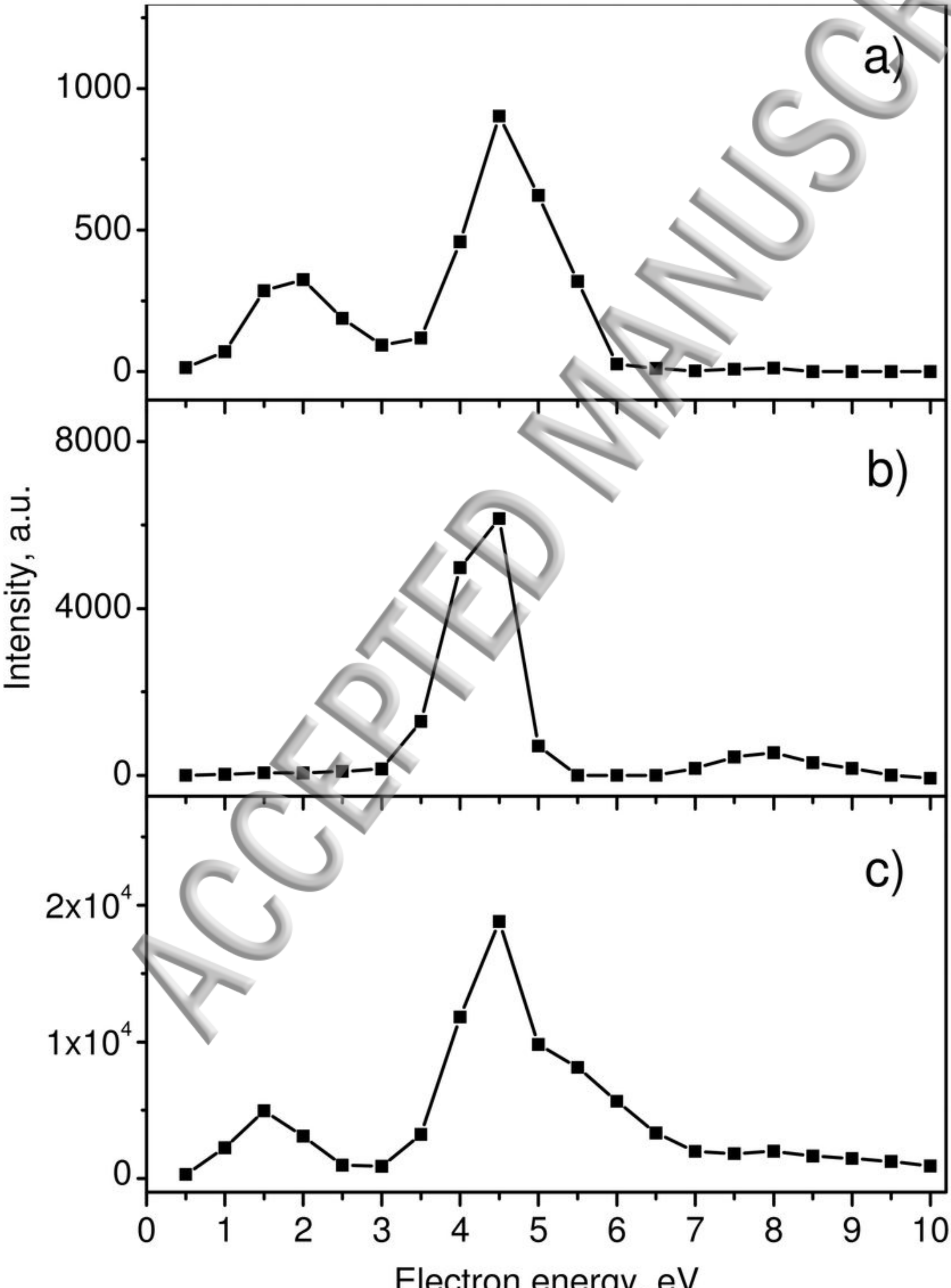
a)
b)
c)
1000
500
0
8000
4000
0
2x10^4
1x10^4
0
Intensity, a.u.
0 1 2 3 4 5 6 7 8 9 10
Electron energy, eV

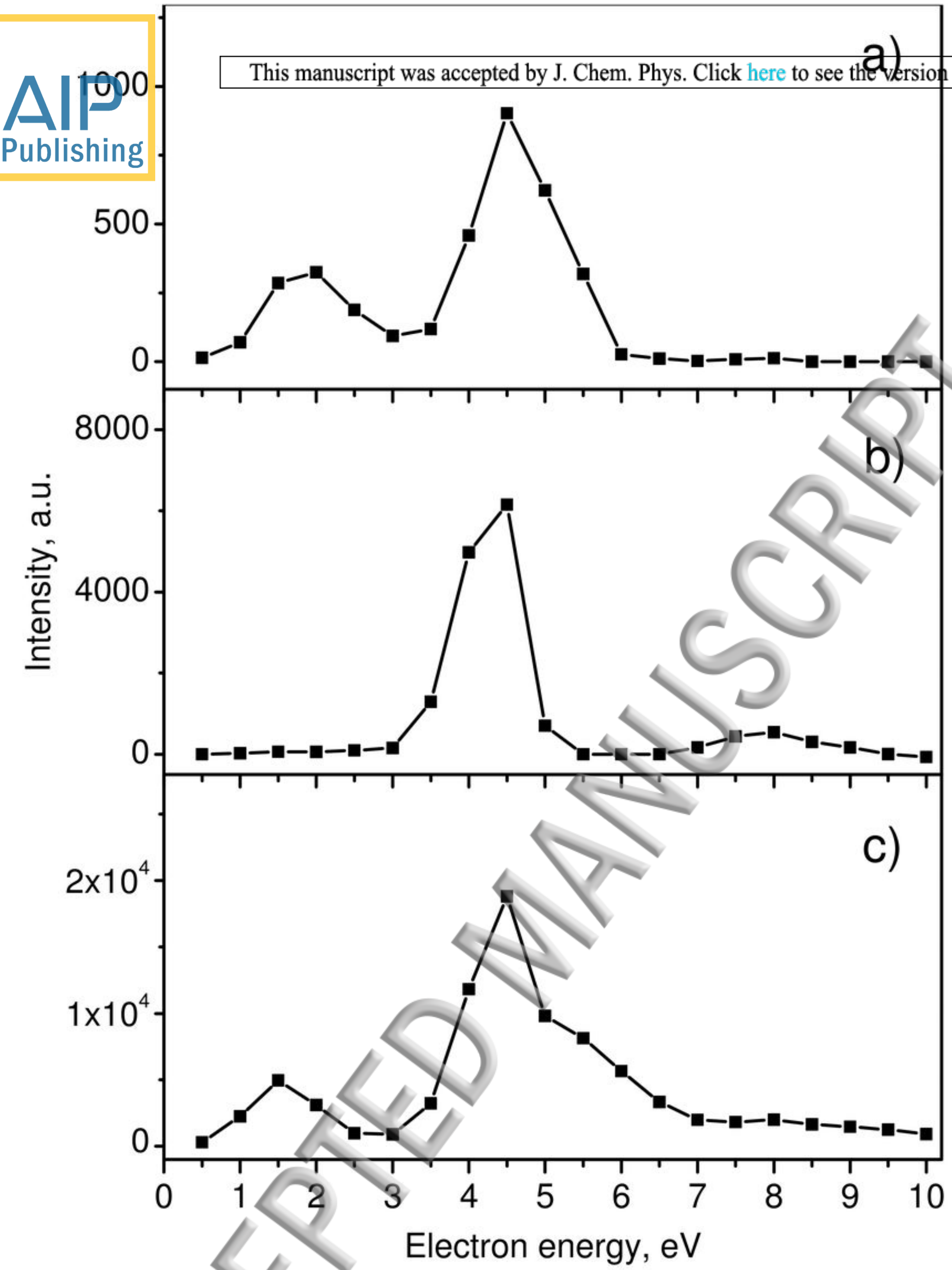
a)
1000
500
0
b)
8000
4000
0
c)
2x10^4
1x10^4
0
Intensity, a.u.
0
1
2
3
4
5
6
7
8
9
10
Electron energy, eV

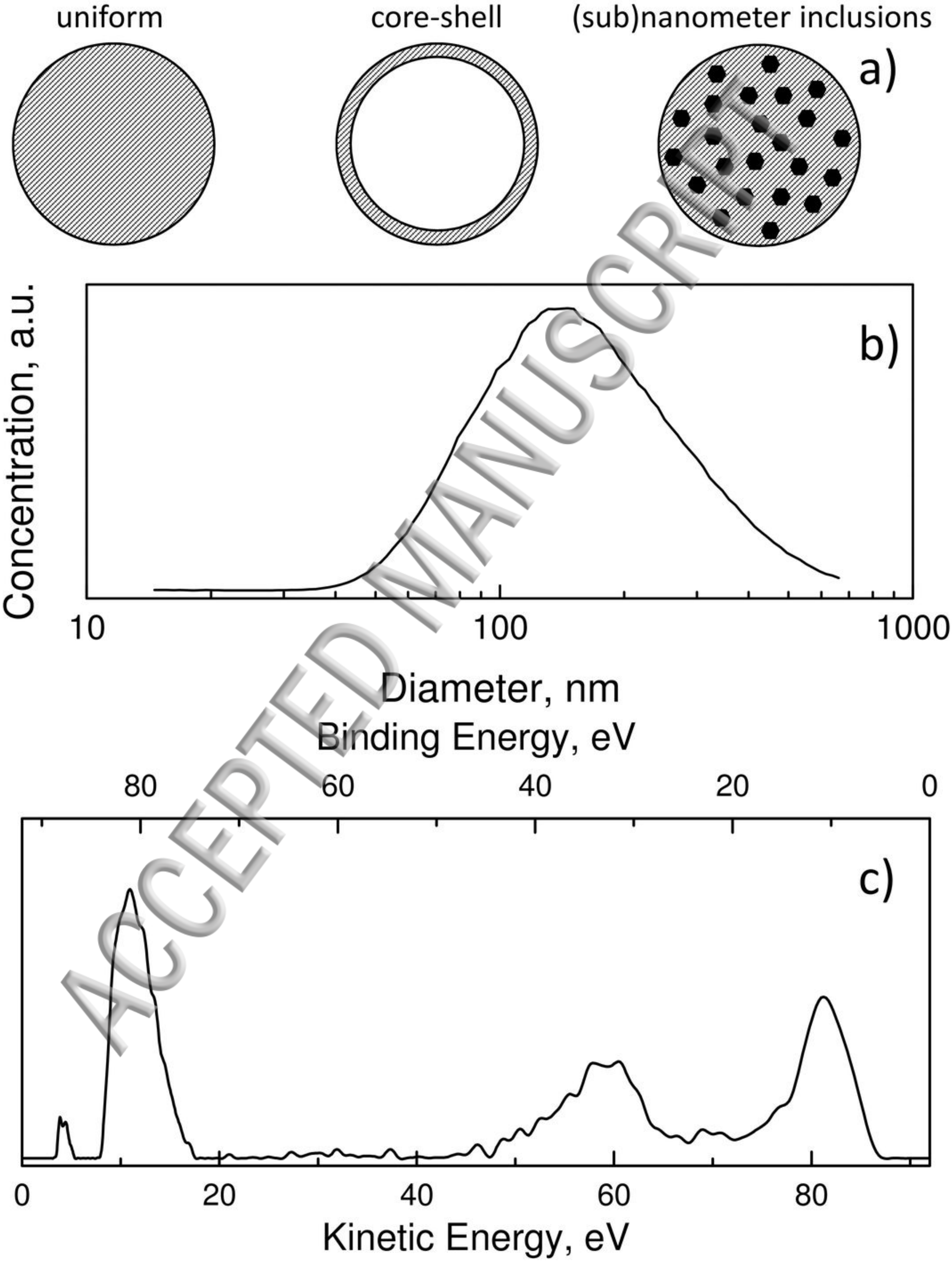
uniform
core-shell
(sub)nanometer inclusions
a)
b)
Concentration, a.u.
10
100
1000
Diameter, nm
Binding Energy, eV
80
60
40
20
0
c)
Intensity, a.u.
0
20
40
60
80
Kinetic Energy, eV

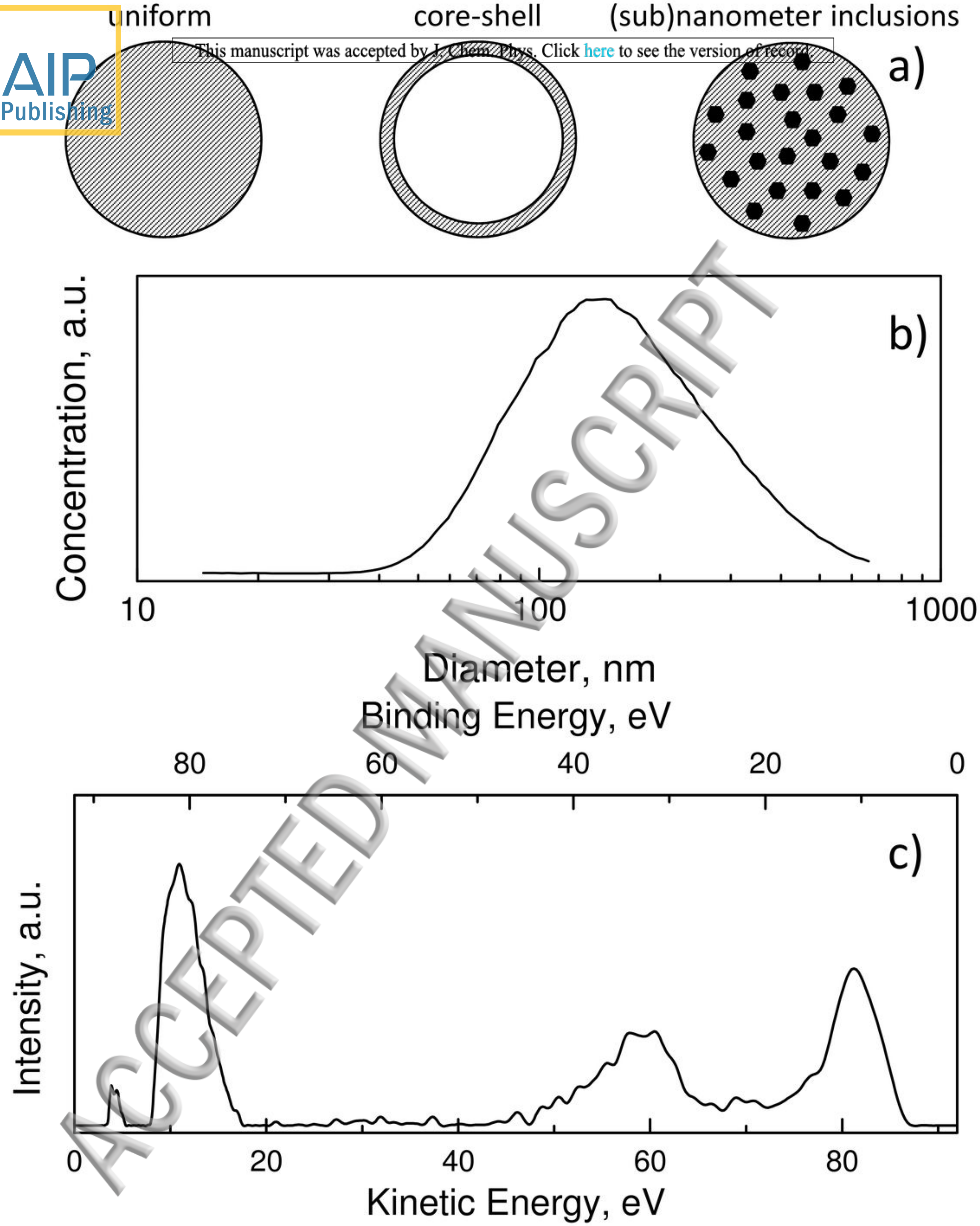
uniform
core-shell
(sub)nanometer inclusions
a)
b)
Concentration, a.u.
10
100
1000
Diameter, nm
Binding Energy, eV
80
60
40
20
0
c)
Intensity, a.u.
0
20
40
60
80
Kinetic Energy, eV